Highlights:

- 4D quantification of growing clinopyroxene and plagioclase crystals
- Temperature and time control the nucleation of pyroxene and plagioclase in basalts
- Investigation of the crystal effect on the rheology and transport of basaltic lava
- Reproduction of the final solidification history of the 2001 Etna lavas
- Application of real-time synchrotron X-ray imaging to forecast lava flow hazards

In situ quantification of crystallisation kinetics of plagioclase and clinopyroxene in basaltic magma: implications for lava flow

Nolwenn Le Gall[1,2*], Fabio Arzilli[3], Giuseppe La Spina[3], Margherita Polacci[3], Biao Cai[4], Margaret E. Hartley[3], Nghia T. Vo[5], Robert C. Atwood[5], Danilo Di Genova[6], Sara Nonni[7], Edward W. Llewellin[8], Mike R. Burton[3], Peter D. Lee[1,2]

[1]Department of Mechanical Engineering, University College London, London, WC1E 7JE, UK

[2]Research Complex at Harwell, Rutherford Appleton Laboratory, Harwell, Oxfordshire, OX11 0FA, UK

[3]Department of Earth and Environmental Sciences, University of Manchester, Manchester, M13 9PL, UK

[4]School of Metallurgy and Materials, University of Birmingham, Birmingham, B15 2TT, UK

[5]Diamond Light Source Ltd., Didcot, OX11 0DE, UK

[6]Bayerisches Geoinstitut, Universität Bayreuth, 95440 Bayreuth, Germany

[7]University of Manchester at Harwell, Didcot, OX11 0DE, UK

[8]Department of Earth Sciences, Durham University, Durham, DH1 3LE, UK

*n.gall@ucl.ac.uk

Abstract

Crystallisation is a complex process that significantly affects the rheology of magma, and thus the flow dynamics during a volcanic eruption. For example, the evolution of crystal fraction, size and shape has a strong impact on the surface crust formation of a lava flow, and accessing such information is essential for accurate modelling of lava flow dynamics. To investigate the role of crystallisation kinetics on lava flow behaviour, we performed real-time, *in situ* synchrotron X-ray microtomography, studying the influence of temperature-time paths on the nucleation and growth of clinopyroxene and plagioclase in an oxidised, nominally anhydrous basaltic magma. Crystallisation experiments were performed at atmospheric pressure in air and temperatures from 1250 °C to 1100 °C, using a bespoke high-temperature resistance furnace. Depending on the cooling regime (single step *versus* continuous), two different crystal phases (either clinopyroxene or plagioclase) were produced, and we quantified their growth from both global and individual 3D texture analyses. The textural evolution of charges suggests that suppression of crystal nucleation is due to changes in the melt composition with increasing undercooling and time. Using existing viscosity models, we inferred the effect of crystals on the viscosity evolution of our crystal-bearing samples to trace changes in rheological behaviour during lava emplacement. We observe that under continuous cooling, both the onsets of the pāhoehoe-ʻaʻā transition and of non-Newtonian behaviour occur within a shorter time frame. With varying both temperature and time, we also either reproduced or approached the clinopyroxene and plagioclase phenocryst abundances and compositions of the Etna lava used as starting material, demonstrating that real-time synchrotron X-ray tomography is an ideal approach to unravel the final solidification history of basaltic lavas. This imaging technology has indeed the potential to provide input into lava flow models and hence our ability to forecast volcanic hazards.

Keywords

X-ray microtomography, Basalt, Crystallisation, Lava flow

1. Introduction

Nucleation and growth of crystals are complex processes that dramatically affect the evolution of textures in cooling magmas, and therefore the eruptive dynamics. These processes have been extensively studied, but mainly *ex situ* using laboratory cooling and decompression experiments (e.g. Mollo and Hammer, 2017, for a review; Giuliani et al., 2020, and references therein) and through the textural analysis of both experimental and eruptive products from two-dimensional (2D) and three-dimensional (3D) methods (e.g. Baker et al., 2012, and references therein). Until very recently, there was a paucity of *in situ* data (Ni et al., 2014; Schiavi et al., 2009). Thanks to the emerging developments of X-ray synchrotron imaging techniques and *in situ* apparatus (e.g. Azeem et al., 2017; Drakopoulos et al., 2015), we can now directly capture the progressive development of a crystal texture in 4D (Arzilli et al., 2019; Polacci et al., 2018; Tripoli et al., 2019), i.e. three spatial dimensions plus time, which provides a deeper understanding of magma crystallisation and solidification during flow emplacement.

Pāhoehoe and ʻaʻā are the two most common surface morphologies in basaltic lava flows, with smooth and rough textures, respectively (e.g. Wentworth and Macdonald, 1953; Peterson and Tilling, 1980). Most lavas initially erupt as pāhoehoe and may evolve to ʻaʻā during the progress of the flow. This irreversible transition (e.g. Hon et al., 2003) occurs dominantly in response to the increase in viscosity that, in turn, is controlled by the chemical

evolution of the residual melt, oxygen fugacity conditions and the increase in crystallinity with distance from the vent (e.g. Cashman et al., 1999; Peterson and Tilling, 1980; Vona et al., 2011). Thus, pāhoehoe lavas are typically less crystalline (<25–30 vol% vs >35 vol%) and less viscous than ʻaʻā lavas.

Here, we studied and quantified *in situ* the nucleation and growth kinetics of pyroxene and plagioclase, the two most common phenocrysts in basaltic magmas. These phenocrysts were produced during single-step and continuous cooling experiments, to evaluate the effect of varying both temperature and time on crystal texture. Specifically, we monitored the evolution of the volume fraction, size and shape of clinopyroxene and plagioclase phenocrysts. We also determined the rheology of the crystal-bearing samples for an accurate modelling of lava flow behaviour. Polacci et al. (2018) and Arzilli et al. (2019) partially presented the single-step cooling experiments. Polacci et al. (2018) quantified the disequilibrium crystallisation of clinopyroxene and titanomagnetite using an empirical model accounting for the volume fraction of crystals, while Arzillli et al. (2019) show that rapid (in minutes) crystallisation can trigger magma fragmentation in highly explosive basaltic eruptions. In this work, we present new data that enables us to (1) quantify the 3D growth of individual clinopyroxenes and plagioclases, (2) infer the evolving rheology of the crystal-bearing samples, and (3) compare the crystallisation kinetics induced under different cooling pathways. As such, this work contributes to a better understanding of the final solidification history of lava flows at basaltic volcanoes.

2. Material and Methods

2.1. *Starting material*

A sample suite from the Lower Vents (LV, 2500 m and 2100 m vents) of the 2001 eruption of Mt. Etna, Italy (ET01, Table 1), was used as the starting material for the *in situ* cooling experiments. The erupted trachybasaltic lava (47.7 wt% SiO_2, 5.3 wt% Na_2O+K_2O, Corsaro et al., 2007) contains phenocrysts of clinopyroxene (8–14 vol%), plagioclase (4–7 vol%), olivine (1–3 vol%) and titanomagnetite (less than 1 vol%). Most of the clinopyroxene crystals are subhedral and sub-millimeter in size; others range from 3 to 10 mm. Plagioclase crystals are euhedral and sub-millimeter in size; millimeter crystals are rare (Corsaro et al., 2007).

The rock sample was crushed, placed in a platinum (Pt) crucible and melted in a 1 atm Nabertherm $MoSi_2$ box furnace at 1400 °C for 4 h in air. The process was repeated twice. The melt was then quenched by pouring it onto a steel plate, before being cored into glass cylinders measuring 2.8 mm in diameter × 4 mm in length. The composition of the anhydrous starting glass was measured by Electron probe microanalysis (EPMA) (Table 1).

2.2. *Experimental approach*

Two types of cooling-driven crystallisation experiments were carried out, defined by either (1) a large drop in temperature followed by a dwell time of 4 h at the target temperature (*single-step cooling* SSC) or (2) a continuous temperature decrease at a constant rate (*continuous cooling* CC). These experiments were performed at the I12 beamline of the Diamond Light Source (DLS, Harwell campus, United Kingdom) using the Alice high temperature (max 1460 °C) resistance furnace with controlled heating/cooling rate (max 24 °C/min; Azeem et al., 2017). The cylindrical samples were contained in alumina (Al_2O_3) holders (inner diameter 3 mm, wall thickness 0.5 mm) that were fitted on top of an Al_2O_3 rod attached to the rotation stage, as shown in the sketch in Fig. 1. During the experiments, the

116 temperature was monitored to ± 5 °C by two type R thermocouples placed close to the
117 sample holder.

118 All experiments were performed in air, at ambient pressure and a temperature ranging
119 between 1100 °C and 1250 °C to simulate lava flows at near-vent conditions. The
120 experimental procedure (Fig. 2, Table 2) consisted of an initial constant heating (at 24
121 °C/min) of the sample up to 1250 °C, which is above the liquidus temperature, and a 30 min
122 isothermal hold to ensure the sample was completely melted and homogeneous. The sample
123 was then either cooled as rapidly as possible (24 °C/min) to 1170 °C (experiment SSC1170)
124 or 1150 °C (experiment SSC1150) and held at constant temperature for 4 h, or cooled at a
125 controlled rate of 0.5 °C/min to 1100 °C (experiment CC0.5), before cooling down to room
126 temperature (at 24 °C/min). The choice of a cooling rate of 0.5 °C/min is within the range of
127 estimated rates at which basaltic lava flows cool (0.01–15 °C/min, Cashman et al., 1999;
128 Witter and Harris, 2007).

129 During cooling-induced crystallisation, synchrotron X-ray tomography was conducted in
130 phase-contrast mode with a detector-sample distance of 2300 mm, in order to visualise and
131 analyse in real-time the nucleation and growth of crystals. X-ray tomographic images were
132 acquired using a 53 keV monochromatic X-ray beam and a high-speed camera, providing a
133 field of view of 8 × 7 mm^2 and a pixel size of 3.2 μm. In each scan dataset, a series of 1800
134 projections were acquired over a 180° rotation with an exposure time of 0.05 s per projection.
135 For each crystallisation experiment, up to 80 datasets were captured at a temporal resolution
136 of 3 min per scan, from before the end of sample melting/homogenisation at 1250 °C to the
137 final cooling down to room temperature.

138

139 2.3. *Analytical methods*

140 *2.3.1. Textural analysis*

141 Diamond Light Source in-house scripts derived from the Python-based framework TomoPy
142 (Gursoy et al., 2014) were used to reconstruct the tomographic datasets, including flat-field
143 correction, centre determination (Vo et al., 2014) and the removal of ring artefacts (Titarenko
144 et al., 2010) and blobs (Vo et al., 2018).

145 The reconstructed images were then processed using ImageJ (Abramoff et al., 2004, Fiji
146 Version 1.0) and Avizo (ThermoFisher Scientific, Version 9.4) software. ImageJ was first
147 used to reduce the size of the images to 8-bit, adjust brightness and contrast to highlight the
148 phenocrysts, and crop a Volume of Interest (VoI, 692×726×606–814 voxels) that contains
149 either clinopyroxene or plagioclase crystals. The VoI was chosen to exclude the top air/melt
150 interface meniscus and the trapped air bubbles at the bottom and edges of the sample
151 container (Fig. A.1a). All subsequent analysis was performed in Avizo (Fig. A.2). Noise
152 reduction was achieved by successively applying bilateral and median filters in 3D, in order
153 to efficiently segment crystals.

154 Crystals were segmented with interactive thresholding, and successively dilating, eroding
155 and/or opening the segmented volumes, as well as removing small particles (mainly oxides).
156 A large part of the oxides had to be removed manually due to the difficulty of automatically
157 identifying and separating them from the clinopyroxene and plagioclase phenocrysts. Three
158 scan datasets per experiment (9 in total) were selected, representing three different steps of
159 the crystallisation process at t_1 = 60 min, t_2 = 160 min and t_3 = 200 min after the start of the
160 dwell/cooling time (t_0).

161 In addition to quantify the mineral abundances (Table 2 and Fig. 3), a total of 10
162 clinopyroxenes in SSC1150 and 10 plagioclases in CC0.5 (Fig. A.3), located in various
163 places in the VoI, were isolated to measure their size (3D length L_{3D}) and volume (V), in

order to assess their growth rate in non-volumetric (Y_{L3D}) and volumetric (Y_V) terms (Figs. 4–6, Tables 2, A.2 and A.3). Changes in crystal length/width aspect ratios (r_p) were also quantified over time, with both the crystal length (Length3D) and width (Width3D) automatically calculated as the longest and shortest Feret diameters, respectively. Most of the segmented crystals were connected, corresponding to aggregates of single crystals (Polacci et al., 2018), so no crystal number density is given.

2.3.2. Chemical analysis

Run products were analysed for their chemistry. Glass, titanomagnetite, clinopyroxene and plagioclase crystals were analysed by EPMA using a Jeol JXA 8530F electron microprobe at the University of Manchester, UK. Analyses were performed using a 15 kV accelerating voltage, 10 nA beam current and beam size of 10 μm. See Polacci et al. (2018) for more details on the procedure.

3. Results

3.1. Mineral assemblages and crystal abundances

All experimental charges contain crystals of titanomagnetite (Table 2), confirming their oxidised nature. They appeared visible in the melt after 12 and 6 min of the dwell time in the SSC1170 and SSC1150 experiments (Polacci et al., 2018), respectively, and after 60 min of continuous cooling in the CC0.5 experiment (although up to t_2 and reaching 1170 °C the oxide volume fraction is near-zero). The two single-step cooled samples (SSC1170, SSC1150) also contain clinopyroxene phenocrysts of augite composition (Table A.1), while the continuously cooled sample (CC0.5) is characterised by the presence of plagioclase and

187 the absence of clinopyroxene. In both SSC1170 and SSC1150, plagioclase was not able to
188 form after 4 h at constant temperature. It started to grow only in the final cooling to room
189 temperature, at T = 1131–1053 °C for SSC1170 and T = 1112–1073 °C for SSC1150 (Arzilli
190 et al., 2019).

191 In SSC11170, the volume fraction of clinopyroxene is systematically very low (<0.002
192 vol%), with only three distinguishable crystals in the segmented VoI (Fig. 3a–c). They are
193 part of a small number of clinopyroxenes present at the bottom of the sample holder, which
194 appeared after 30 min of dwell time (Polacci et al., 2018) on the surface of an entrapped air
195 bubble and in close contact with alumina (Fig. A.1c). Since no other clinopyroxene crystals
196 nucleated in the rest of the charge within 4 h, the temperature of 1170 °C seems to be very
197 close to the liquidus temperature. Consequently, we defined the liquidus temperature of
198 clinopyroxene at 1170 °C.

199 In SSC1150, the nucleation of clinopyroxene crystals started within the first 12 min of the
200 dwell period (Polacci et al., 2018), preferentially at the air-melt interface and on alumina
201 walls (Fig. A.1b), i.e. heterogeneously. The clinopyroxene volume fraction increases with
202 time, from 1 vol% at t_1 = 60 min up to 9 vol% at t_3 = 200 min (Fig. 3d–f), as well as with
203 reducing temperature by 20 °C, from 1170 °C to 1150 °C (Fig. 3a–f).

204 In CC0.5, we did not observe any phenocryst crystallisation within the first hour of the
205 experiment. Plagioclase crystals started to nucleate and grow at ~1205 °C, i.e. after 90 min
206 from the beginning of cooling. They formed on tiny air bubbles attached to the walls of the
207 container. Afterwards, the volume fraction of plagioclase increased with increasing time and
208 decreasing temperature, reaching 22 vol% at t_3 = 200 min and T = 1150 °C (Fig. 3g–i).
209 Clinopyroxene crystallisation did not occur during the continuous cooling at 0.5 °C/min. A

few tiny crystals were observed in the final unquenched product, suggesting that they formed somewhere during final cooling at 24 °C/min, at temperatures below 1100 °C.

In all three experiments, crystals nucleate mostly between t_1 and t_2 (Fig. 3) and then grow with time and/or cooling, i.e. growth is dominant from t_2 onwards.

3.2. Crystal sizes and growth rates

Compared to previous studies, here we provide individual *in situ* 3D measurements of crystal growth kinetics, contributing to a better understanding of crystallisation processes and, as a consequence, of the solidification of basaltic lava flows.

Clinopyroxene size (L_{3D}) nearly triples with increasing the duration of the SSC1150 experiment, ranging from 90–320 µm at t_1 (60 min dwell) to 150–890 µm at t_2 (160 min dwell) to 250–1090 µm at t_3 (200 min dwell, Fig. 4a, Tables 2 and A.2). Plagioclase L_{3D} doubles with mutually increasing time and decreasing temperature in CC0.5, ranging from 270–520 µm at t_2 to 445–1160 µm at t_3 (Fig. 4b, Tables 2 and A.3). Both the clinopyroxene and plagioclase volumes, averaged over 10 single crystals, increased fivefold from 0.3 to 1.6 $\times 10^{-6}$ cm^3 and from 0.8 to 3.8 $\times 10^{-6}$ cm^3, respectively, during the 140 min hold/cooling from t_1 to t_3 (Fig. 4, Tables 2, A.2 and A.3). The average clinopyroxene growth rate (Y_{L3D}) is nearly constant with time, ranging between 6.9 $\times 10^{-6}$ cm/s (t_1) and 5.8 $\times 10^{-6}$ cm/s (t_3), while the average clinopyroxene volumetric growth rate (Y_V) almost triples between 4.6 $\times 10^{-11}$ cm^3/s (t_1) and 12 $\times 10^{-11}$ cm^3/s (t_3) (Fig. 5, Tables 2 and A.2). Both the average Y_{L3D} and Y_V of plagioclase crystals are more impacted by time and temperature, with Y_{L3D} almost quadrupling (3.7 to 16 $\times 10^{-6}$ cm/s) during 40 min of cooling from t_2 to t_3, and Y_V increasing by a factor of 10 (4.1 to 55 $\times 10^{-11}$ cm^3/s, Fig. 5, Tables 2 and A.3).

3.3. Crystal morphologies

In SSC1150, clinopyroxene crystals formed with a gradual transition from elongated prismatic shapes to multi-branched crystals as growth proceeds (Fig. 4a; Polacci et al., 2018; Arzilli et al., 2019). Spherulitic morphologies were also observed, corresponding to heterogeneously nucleated crystal aggregates similar to that reported by Arzilli et al. (2015) for alkali feldspars. Plagioclase crystals from the CC0.5 run product exhibit an elongate bladed habit (Fig. 4b). No change in morphology was observed with increasing time and decreasing temperature, although crystals become more elongated and branched. We observed a morphological difference in the iron oxides that exhibit an equant shape under single-step cooling (in SSC1150) and a skeletal form under continuous cooling (in CC0.5).

4. Discussion

4.1. Single-step versus continuous cooling: differences in mineralogical assemblages and kinetics

4.1.1. Mineralogical differences

Depending on the type of cooling (single-step vs continuous), we noticed the presence or absence of clinopyroxene and plagioclase. Clinopyroxene is present in both single-step experiments, although in a very small amount in SSC1170, from near the beginning of the dwell period (after 12 min dwell in SSC1150, Polacci et al., 2018), while plagioclase remains absent until the final cooling stage (Arzilli et al., 2019), occurring as skeletal crystals. On the contrary, only plagioclase crystallised from the melt on continuous cooling (CC0.5), with the occurrence of minor clinopyroxenes (too small for analysis by EPMA) during the final

cooling to room temperature. For comparison, the equilibrium assemblage calculated by MELTS software (Ghiorso and Sack, 1995; Asimow and Ghiorso, 1998), at ambient pressure and fugacity (magnetite-hematite MH redox buffer), comprises both plagioclase ($T_{liquidus}$ = 1208 °C) and clinopyroxene ($T_{liquidus}$ = 1188 °C). As discussed above (section 3.1), the texture of the SS1170 charge suggests that the liquidus temperature of clinopyroxene is closer to 1170 °C. This enabled us to determine the nucleation undercooling ($\Delta T = T_{liquidus} - T_{experimental}$) as a function of temperature: for clinopyroxene ΔT = 0 °C at 1170 °C and 20 °C at 1150 °C, for plagioclase ΔT = 0 °C at 1220 °C, 38 °C at 1170 °C and 58 °C at 1150 °C. Both the SSC1170 and SSC1150 experiments were thus run below the predicted plagioclase liquidus, meaning that plagioclase should have been present within the 4-h dwell. Similarly, we performed part (80 min) of the CC0.5 experiment below the clinopyroxene liquidus without nucleating clinopyroxene crystals. In each cooling regime, the nucleation of one crystal phase is suppressed, attesting to disequilibrium crystallisation.

The absence of either plagioclase or clinopyroxene in cooling-induced crystallisation experiments, while it should be thermodynamically stable, was reported previously by some authors (e.g. Corrigan, 1982; Gibb, 1974; Lofgren, 1983; Vetere et al., 2015). They mainly attribute the failure of these phases to nucleate to the degree of undercooling (a large ΔT, or high cooling rate, inhibiting the nucleation of plagioclase), a limited experimental duration and a low number of heterogeneous nucleation sites. In our SSC1150 single-step experiment, the nucleation of clinopyroxene followed a rapid (24 °C/min) temperature drop that drove a rapid increase of undercooling to 20 °C for clinopyroxene and to 58 °C for plagioclase, and brought the melt to sub-liquidus conditions where both phases can grow. However, although the nucleation of clinopyroxene was activated after 12 min at constant temperature, plagioclase was not able to crystallise within the 4 h dwell. This indicates first that time plays

a major role in the evolution of crystallisation, and second that clinopyroxene needs lower activation energy to nucleate, associated with its lower number of tetrahedral units (Al–O and Si–O bonds) and less polymerised structure in comparison to plagioclase, which in turn translates into a shorter delay in nucleation (Iezzi et al., 2008). In addition, following these relatively fast nucleation and growth, the residual melt became depleted in clinopyroxene components (Ca, Mg, Fe, Table A.1), possibly delaying the stabilization of plagioclase nuclei. In contrast, and despite its more complex structure, the slow cooling rate of 0.5 °C/min enabled the nucleation of plagioclase. This suggests that suppression of crystal nucleation is not simply related to structural control alone, as previously suggested by Corrigan (1982). Following the nucleation and growth of plagioclase crystals near the liquidus temperature, the residual melt became depleted in plagioclase components (anorthite: Ca and Na, Table A.1), creating a local disequilibrium that may have delayed the formation of clinopyroxene. Nucleation sites for clinopyroxene may also be missing. They may have been suppressed because of a longer time spent above their liquidus temperature (122 min for CC0.5 instead of 3 min for SSC1150, from the end of melting/homogenisation) or occupied by early-formed plagioclase crystals.

Our observations show that the cooling rate and the resulting increase of undercooling through time are important factors controlling crystallisation. In this sense, Vetere et al. (2015) documented that plagioclase is only able to crystallise at low to moderate cooling rates (< 3 °C/min). However, Arzilli et al. (2019) observed the crystallisation of plagioclase at a high cooling rate of 24 °C/min. The difference may be related to initial conditions, since superheating, as applied by Vetere et al. (2015), can promote an efficient dissolution of pre-existing nuclei (e.g. Arzilli et al., 2015), while a time-step at sub-liquidus conditions can promote the formation of stable nuclei, which once subjected to a rapid thermal perturbation of the system are able to grow rapidly. The effects of thermal history on the mineralogical

assemblage of cooling basalts appear to be not yet well understood, stressing that more systematic real-time investigations should be performed.

4.1.2. Crystal nucleation kinetics

The experimental charges have higher crystal abundances at the gas-melt and container-melt interfaces because of the lower surface free energy required for nucleation. At the container walls, the heterogeneous nucleation of plagioclase and clinopyroxene crystals is associated with the presence of tiny air bubbles and the early formation of Al–Mg oxides (Fig. A.4), both acting as nucleation sites. The presence of pre-existing nuclei is an important mechanism that contributes to the solidification of basaltic lava flows (e.g. Mollo et al., 2015), emphasising that *in situ* observations can unravel the dynamics of heterogeneous crystal nucleation and its important implications on the development of basaltic textures, and so on conduit processes and eruptive dynamics.

In addition to being reduced by heterogeneous nucleation, the nucleation delay, i.e. the time between when the melt is brought below its liquidus and the onset of nucleation (Rusiecka et al., 2020), is reduced as a function of undercooling. As expected with increasing undercooling and/or experimental duration (e.g. Rusiecka et al., 2020 and references therein; Vona and Romano, 2013), the nucleation of clinopyroxene occurs faster and the volume fraction of crystals increases (Fig. 3). The plagioclase-free texture of the SSC1150 sample, during the 4-h dwell, is also consistent with the findings of Rusiecka et al. (2020).

In contrast to previous *in situ* research (Ni et al., 2014) that reports the nucleation of olivine or clinopyroxene crystals only in a short event of a few minutes at the beginning of the experiment, we observed multiple nucleation events up to t_2 (160 min dwell/cooling) and the

continuous growth of both clinopyroxene (SSC1150) and plagioclase crystals (CC0.5). These multiple nucleation events, reported as two main nucleation/growth pulses in SSC1150 (at 60 and 150 min dwell) in Polacci et al. (2018), may be induced by changes in melt composition with further effects on the liquidus temperature, following the nucleation and growth of first crystals. Such multiple nucleation events have been recently reported by Giuliani et al. (2020) to account for the formation of clinopyroxene in basaltic melt.

4.1.3. Crystal growth kinetics

In the time interval of our experiments, clinopyroxene and plagioclase crystals grew at rates of 10^{-6} cm/s and 10^{-5}–10^{-6} cm/s, respectively. A clinopyroxene growth rate of 10^{-6} cm/s is similar to, or higher than, the one reported in previous works on anhydrous basaltic and trachybasaltic melts (10^{-6}–10^{-9} cm/s, Baker, 2008; Burkhard, 2005; Giuliani et al., 2020; Ni et al., 2014; Orlando et al., 2008; Pontesilli et al., 2019). Lower growth rates of 10^{-7}–10^{-9} cm/s have been reported for plagioclase crystals (Arzilli et al., 2015; Giuliani et al., 2020; Orlando et al., 2008). These differences are associated with the use of *in situ* data, since we measured dynamic growth rates that are known to decrease with increasing dwell time (e.g. Pontesilli et al., 2019), with impingement by surrounding crystals. *Ex situ*, growth rates are determined for entire experimental periods and are thus averaged and possibly underestimated. In addition, the use of 2D data provides less accurate shape information.

At constant undercooling (ΔT = 20 °C), the clinopyroxene growth rate by size (Y_{L3D}) is nearly constant through time, and the volumetric growth rate (Y_v) slightly increases (Fig. 5). With increasing undercooling by 20 °C, from 38 °C to 58 °C, both the Y_{L3D} and Y_v plagioclase growth rates quadruple (Fig. 5). Kirkpatrick (1975) also showed an increase of the rate of crystal growth with increasing undercooling for a large temperature range.

Following Tamman (1899) and as predicted by the theory (Kirkpatrick, 1975), we can expect the rate of crystal growth to be near-zero at the liquidus, increase to a maximum and then decrease with increasing undercooling.

The initially individual clinopyroxene and plagioclase crystals grew along thermodynamically favourable directions, i.e. perpendicular to the surface of heterogeneities (Al-walls of the sample holder, air bubbles and first-nucleated crystals, including many oxides), forming networks of agglomerated crystals (Fig. 3). Clinopyroxene crystals grew radially from the top of the VoI and the edge walls of the alumina container, mainly by branching and aggregation (Fig. 3d–f). Plagioclases also align along preferential directions, perpendicular to the sample holder (Fig. 3g–i). The euhedral textures developed by both the clinopyroxenes and titanomagnetites in SSC1150 result from interface-controlled growth mechanisms, which are favoured by a small undercooling of 20 °C and a high temperature of 1150 °C that is close to the liquidus temperature of 1170 °C. In contrast, the plagioclase blades observed in CC0.5 indicate some disequilibrium between the melt and crystals, linked to larger undercoolings and departure from their liquidus temperature (1208 °C). The shape of these rapidly growing crystals is controlled by diffusion, with a slow diffusivity of cations in the melt (Mollo and Hammer, 2017). Attainment of equilibrium did not occur during the course of the continuous cooling experiment (~5 h) for plagioclase. In that experiment, the oxide crystals are skeletal, which also attests to their development under conditions of rapid growth and high degrees of undercooling.

Aggregation of smaller and mutually touching crystals was reported to occur in Etnean pāhoehoe and ʻaʻā lavas at syn-eruptive conditions over the effect of undercooling (e.g. Lanzafame et al., 2013). This underlines the close reproducibility of the near-surface crystallisation of basaltic melts by our innovative *in situ* approach and thus its utility in lava flow studies.

377

378 *4.1.3. Rheology of the crystal-bearing samples*

379 Growing crystals increase the viscosity of the suspending basaltic lava and introduce non-
380 Newtonian rheology (e.g. Giordano et al., 2008; Mueller et al., 2010; Vona et al., 2011),
381 which in turn affects its transport (e.g. Soldati et al., 2016). Assessing the rheological
382 evolution of crystallising basaltic melts is thus required for lava flow modelling, to predict
383 how the lava flow will evolve in time and space. Here, we infer the evolving rheology of our
384 SSC1150 and CC0.5 crystal-bearing samples from a Hershel-Bulkley model (Herschel and
385 Bulkley, 1926; Mader et al., 2013):

$$\tau = \tau_0 + K\dot{\gamma}^n \,, \qquad \text{Eq. 1}$$

386 where τ is the shear stress, τ_0 is a yield stress, K is the consistency, $\dot{\gamma}$ is the strain-rate and n
387 is the flow index. The rheological impact of the crystal phase depends primarily on the ratio
388 of the crystal volume fraction ϕ to the maximum crystal packing fraction ϕ_m (ϕ/ϕ_m)
389 because τ_0, K and n are all functions of ϕ/ϕ_m (Mader et al., 2013). ϕ_m can be calculated
390 from the aspect ratio of the crystals r_p (Mader et al., 2013; Mueller et al., 2010):

$$\phi_m = 0.55 \exp\left[-\frac{\left(\log_{10} r_p\right)^2}{2}\right]. \qquad \text{Eq. 2}$$

391 Both ϕ and r_p are measured directly from our *in situ* data (Section 2.3.1). SSC1150 contains
392 clinopyroxene crystals with average aspect ratios of 4.07 (60 min dwell), 7.41 (160 min
393 dwell) and 7.35 (200 min dwell, Tables 2 and A.2), and CC0.5 contains plagioclase crystals
394 with average r_p of 4.24 (160 min cooling) and 5.76 (200 min cooling, Tables 2 and A.3).
395 Consistency and flow index are calculated following Mader et al. (2013):

$$K = \mu_0 \left(1 - \frac{\phi}{\phi_m}\right)^{-2}, \quad \text{Eq. 3}$$

$$n = 1 - 0.2 r_p \left(\frac{\phi}{\phi_m}\right)^4, \quad \text{Eq. 4}$$

where μ_0 is the viscosity of the melt phase, which can be calculated as a function of composition and temperature (Giordano et al., 2008). At 1170 °C and 1150 °C, the viscosities of melt samples are respectively of 2.01 and 2.18 log Pa s. Computed values of ϕ_m, the ratio ϕ/ϕ_m, K and n are tabulated in Table 2.

Mader et al. (2013) show that τ_0 is negligible for $\phi/\phi_m < 0.8$, which is the case for all of our tomographic reconstructions. In this case, Equation 1 reduces to a power law in which suspension viscosity η depends on strain rate:

$$\eta = K\dot{\gamma}^{n-1}. \quad \text{Eq. 5}$$

They further argue that shear thinning effects can be neglected for most strain rates of practical interest if $n \geq 0.9$, which is the case for most of our tomographic reconstructions. In this case, $\eta \equiv K$ and the Newtonian suspension viscosity can be calculated directly using Equation 3.

Results (Tables 2, A2 and A3) show that our samples exhibit a Newtonian behaviour during both the dwell and continuous cooling, with small ϕ/ϕ_m of 0.02 at t_1 to 0.24 at t_3 in SSC1150 and of 0.20 at t_1 to 0.53 at t_3 in CC0.5, respectively. However, higher values of this ratio (0.64 in SSC1150 and 0.58 in CC0.5) are expected after more than the 200 min dwell/cooling, by considering a maximum ϕ of 0.24 as found in the LV magmas (Corsaro et al., 2007). With more time, our two samples produced under different temperature-time conditions, would thus evolve towards a non-Newtonian behaviour, with consequences for magma transport (see Section 4.2).

Magma viscosity is also dependent on shear rate, which facilitates the nucleation and growth of crystals (Vona and Romano, 2013). During transport and emplacement, magmas and lavas undergo a range of shear rates (2.5–0.001 s^{-1}, Kolzenburg et al., 2018 and references therein). Although we did not investigate the effect of varying the deformation rate on the rheological evolution of crystallising basaltic melts, previous experimental studies (Kolzenburg et al., 2018; Tripoli et al., 2019; Vona et al., 2011; Vona and Romano, 2013) showed that shear deformation accelerates crystallisation kinetics, resulting in shorter nucleation delays and higher crystal fractions.

In more detail, Vona et al. (2011) performed *ex situ* isothermal crystallisation experiments while capturing the temporal evolution of the viscosity of anhydrous Etna basalt of the 1991–1993 eruption deformed under a low strain rate of 0.53 s^{-1}. In air, at 1157 °C and 1 atm, crystallisation takes place within 29–45 h, associated with an increase in apparent viscosity to a stable value of 3.07 log Pa s (ϕ = 0.16). The final mineralogical assemblage is composed of spinel (minor) and plagioclase, which differs from our SSC1150 experiment, where clinopyroxene nucleated after a short 12-min delay. Their starting melt composition slightly differs from ours, but not enough to justify such a difference in crystallisation time, as well as in the order of nucleation of crystal phases. We suggest, instead, that these differences can be explained by a longer time spent above the liquidus temperature (5h at 1400 °C in Vona et al., 2011 vs 30 min at 1250 °C in our study), which allows a more complete dissolution of pre-existing nuclei. These differences can also be explained by the use of a different apparatus (concentric cylinder viscometer) equipped with a spindle that causes chemical heterogeneities and mechanical perturbations in the melt (Vona et al., 2011). Recent findings (e.g. Tripoli et al., 2019; Kolzenburg et al., 2020) demonstrated that in the absence of thermal and/or mechanical fluctuations the nucleation of plagioclase is not favoured, as observed in our single-step experiments.

Using the model of Vona et al. (2011), which considers the magma strain rate and both the crystal fraction and crystal shape factors (Vona and Romano, 2013), we calculated the relative viscosity of our SSC1150 suspensions (liquid + crystal, considering both clinopyroxene and oxide phases). As expected (Vona et al., 2011 and references therein), the relative viscosity increases with increasing crystal fraction ϕ, from 1.21 log Pa s at ϕ = 0.05 (t_1, Table 2) to 2.39 log Pa s at ϕ = 0.14 (t_2, Table 2) to 3.37 log Pa s at ϕ = 0.17 (t_3, Table 2). According to Polacci et al. (2018), a stable clinopyroxene crystal content (~14 vol%) can be reached after ~500–1500 min dwell (~8–25 h) in the SSC1150 sample, which translates to a higher relative viscosity of 6.93 log Pa s at ϕ = 0.22 (including a stable oxide content of 8 vol%, Arzilli et al., 2019).

Kolzenburg et al. (2018) were among the first to study the effect of shear rate at non-isothermal conditions, which can be related to our CC0.5 continuous cooling experiment. They observed that the onset temperature of crystallisation increases with increasing shear rate, from 1101 °C (no shear) to 1164 °C and 1178 °C for shear rates of 1.16 and 4.64 s^{-1}, respectively, at a cooling rate of 0.5 °C/min and using a trachybasalt from the 2013 eruption of Etna. However, in CC0.5 crystallisation occurs at high temperatures (~1205 °C) without introducing shear, suggesting that results can hardly be compared with each other. Here again, differences can be due to the use of a concentric cylinder apparatus with a longer time spent above the liquidus temperature (several hours at 1300 °C) and more reduced conditions, and a slightly different starting melt composition. Kolzenburg et al. (2018) also showed that increasing shear rate increases the cutoff temperature (T_{cutoff}, i.e. the point at which the sample rheologically solidifies and flow stops), which implies shorter flow distances. Although it is not relevant to our data, if deformation is taken into account, transitions between different eruptive styles or flow mechanisms can occur in a shorter amount of time (Vona and Romano, 2013).

4.2. Implications for basaltic lava flows

4.2.1. Time evolution of magma crystallinity: the pāhoehoe-ʻaʻā transition

As described above, our results can be used to investigate the effect of cooling and crystallisation on the rheological properties of lava, and more specifically to retrieve the conditions under which pāhoehoe lavas transform to ʻaʻā. Such a transition is greatly influenced by the viscosity of the lava, which is dependent on temperature and crystallinity, and associated with the development of yield strength (Cashman et al., 1999). A critical crystallinity range at which pāhoehoe transforms to ʻaʻā has been identified between 0.18 and 0.35 (Hon et al., 2003; Soule et al., 2004), although some Etnean pāhoehoe lavas (termed "cicirara") can contain up to 40 vol% crystals (e.g. Lanzafame et al., 2013). We inferred such parallel changes of crystallinity and rheological behaviour (onset of non-Newtonian behaviour) after more than 200 min dwell/cooling at a comparable crystallinity of 0.24, as found in the 2001 trachybasalts. In addition, a critical viscosity range for the pāhoehoe–ʻaʻā transition has been calibrated from a combination of field observations and laboratory experiments, from 4 log Pa s (no shear rate) to ~2.7 log Pa s with increasing shear rate (e.g. Cashman and Mangan, 2014, and references therein; Sehlke et al., 2014; Soldati et al., 2017). In line with this finding, such viscosities are approached in our single-step cooling conditions (SSC1150) after 200 min and largely exceeded within 8 h. Under our given *P*-*T*-fO_2-composition conditions, the transition of basaltic lava from pāhoehoe to ʻaʻā can thus be crossed in ca. 4 h from emission under continuous cooling, or between 3 and 8 h under single-step cooling.

488 *4.2.2. Crystallisation timescales in basaltic lava flows and the case study of the 2001*
489 *eruption of Mt. Etna*

490 Under single-step cooling (near-isothermal) conditions, our data coupled with the empirical
491 model of Polacci et al. (2018) indicate that 14 vol% of crystals (single-phase) can nucleate
492 and grow over a day. This amount alone is not enough to bring a major shift in rheological
493 behaviour, implying that lava can travel great distances with minimal cooling. Under
494 continuous cooling (non-isothermal) conditions, our results demonstrate that the growth of 22
495 vol% plagioclase crystals in just over 3 h would soon have a significant impact on flow
496 behaviour. According to Kolzenburg et al. (2020), the lava could solidify and stop flowing
497 after reaching 1128 °C, i.e. after 244 min (~4 h) of continuous cooling at 0.5 °C/min. During
498 flowage onto the surface, the behaviour of basaltic lavas appears to be greatly influenced by
499 both temperature and time, with crystal phases possibly nucleating and growing under
500 different cooling regimes, as explored below.

501 As a trachybasalt from the 2001 Etna eruption was used as the starting material for our
502 experimental simulations of lava flow emplacement, results can aid in the interpretation of
503 the final crystallisation history of the erupted LV lavas. According to Lanzafame et al. (2013)
504 who unravelled the solidification path of a pāhoehoe lava from Mt. Etna through petrographic
505 analysis, crystals with a size <1 mm (~75 vol%) crystallised during lava emplacement. Our
506 results agree well with this finding, since the SSC1150 single-step cooled sample crystallised
507 the amount of clinopyroxene phenocrysts found in the 2001 lavas (~9–14 vol%) within 200
508 to 500–1500 min of dwell (Polacci et al., 2018) at 1150 °C. After that time, a critical
509 crystallinity (of maximum 24 vol%) could be reached with the appearance of a second
510 phenocryst phase (6–7 vol% plagioclase) in the same proportions as in the 2001 LV products.
511 For comparison, in the CC0.5 sample, continuously cooled at a rate of 0.5 °C/min, 4 to 7
512 vol% plagioclase crystals appeared in less than 160 min at $T \geq 1170$ °C. However, 40 min

later (T = 1150 °C) CC0.5 already contained 22 vol% plagioclase and no clinopyroxene, which differs strongly from the LV products. In addition to reproduce the abundance of clinopyroxene crystals in the SSC1150 experiment, we reproduced their composition with an average Mg number (Mg#) of 72 vs of 73 in the LV products (Fig. 6). According to Mollo et al. (2015), the $Mg\#_{54–74}$ clinopyroxene population in Etna products formed within the range of our experimental conditions, i.e. at 0.1–500 MPa and 1050–1175 °C. LV textures are thus very well reproduced by our single-step experiment at 1150 °C, meaning first that the interior of lava flows in the 2001 eruption may have cooled almost isothermally, and second that the nucleation of clinopyroxene may have occurred in the shallowest portion of the Etnean plumbing system and during lava transport at the surface. However, this excludes the few larger (3–10 mm) clinopyroxene crystals present in the LV lavas, which cannot be reproduced by our experiments, and that result from crystallisation at depth during storage (Mollo et al., 2015 and references therein), as well as olivine crystals that nucleated and grew under water-saturated conditions at high pressures and temperatures (Mollo et al., 2015). The nucleation of plagioclase seems to have happened differently. According to La Spina et al. (2016), the low plagioclase content in the 2001 LV products indicates a fast (<1 h) vertical ascent from depth (9 km) to the surface. Plagioclase crystals might have nucleated and grew during ascent under non-equilibrium conditions, and not during flow advance, driven by magma degassing (Mollo et al., 2015). In accordance with it, both the lower range of plagioclase core compositions and rim compositions (An_{64}, Corsaro et al., 2007) were reproduced in the SSC1150 experiment (An_{67}, Fig. 6 and Table A.1), implying that plagioclases in the LV trachybasalts did not nucleate outside of the conduit, although their growth was affected by subaerial conditions. The interior of the 2001 lava flows could thus result from a combination of pre-, syn- and post-eruptive crystallisation.

As demonstrated with our study, working *in situ* enables the solidification of a basaltic lava flow to be directly observed, and so reproduced with varying both time and temperature. This opens new perspectives to unravel the solidification path of basaltic lavas, especially as only a small amount of phenocrysts could equilibrate at depth, with most of the crystallisation happening during magma ascent in the conduit and emplacement to the surface (Lanzafame et al., 2013; Giuliani et al., 2020), which are conditions that we can simulate with our *in situ* equipment.

5. Conclusions

Our results from single-step *versus* continuous cooling experiments show that cooling rate and undercooling have a strong influence on the nucleation of clinopyroxene and plagioclase, with implications for the behaviour of basaltic lavas. According to our 3D time-dependent observations combined with published rheological data, the interior of the 2001 lava flows of Etna may have crystallised up to 14 vol% clinopyroxene phenocrysts almost isothermally over a day. Such a nucleation and growth of crystals during lava flow emplacement accompanies changes in rheological behaviour, which affect lava flow length and hazard severity.

Acknowledgments

We acknowledge financial support from the 'DisEqm' project (Quantifying disequilibrium processes in basaltic volcanism) and the 'Shedding new light on volcanoes: real time synchrotron X-ray tomography of magmatic phenomena' project, both funded by NERC (NE/N018575/1 and NE/M013561/1). We also acknowledge the use of facilities and support

provided by the Research Complex at Harwell and thank Diamond Light Source, UK, for providing beamtime at the I12 beamline (visit number EE12392), and all staff for technical assistance. PDL acknowledges funding for his Royal Academy of Engineering Chair (CiET1819/10). Many thanks to Mohammed Azeem for his help with the furnace during the beamtime and its preparation, Sebastian Marussi for providing the technical drawings showed in Figure 1 and Stuart McCallum for a review of an early version of this manuscript. The editor Rosemary Hickey-Vargas, and two anonymous reviewers are acknowledged for their comments and suggestions that helped improve this manuscript.

References

Abramoff, M. D., Magalhaes, P. J., Ram, S. J., 2004. Image processing with ImageJ. Biophotonics Int. 11, 36–42.

Arzilli, F., Mancini, L., Voltolini, M., Cicconi, M.R., Mohammadi, S., Giuli, G., Mainprice, D., Paris, E., Barou, F., Carroll, M.R., 2015. Near-liquidus growth of feldspar spherulites in trachytic melts: 3D morphologies and implications in crystallization mechanisms. Lithos. 216–217, 93–105. https://doi.org/10.1016/j.lithos.2014.12.003

Arzilli, F., La Spina, G., Burton, M.R., Polacci, M., Le Gall, N., Hartley, M.E., Di Genova, D., Cai,B., Vo, N.T., Bamber, E.C., Nonni, S., Atwood, R., Llewellin, E.W., Brooker, R.A., Mader,H.M., Lee, P.D., 2019. Magma fragmentation in highly explosive basaltic eruptions induced by rapid crystallization. Nat. Geosci. 12, 1023–1028. https://doi.org/10.1038/s41561-019-0468-6

581 Asimow, P. D., Ghiorso, M. S., 1998. Algorithmic modifications extending MELTS to
582 calculate subsolidus phase relations. Am. Mineral. 83, 1127–1132.
583 https://doi.org/10.2138/am-1998-9-1022

584 Azeem, M. A., Lee, P.D., Phillion, A.B., Karagadde, S., Rockett, P., Atwood, R.C., Courtois,
585 L., Rahman, K.M., Dye, D., 2017. Revealing dendritic pattern formation in Ni, Fe and
586 Co alloys using synchrotron tomography. Acta Mater. 128, 241–248.
587 https://doi.org/10.1016/j.actamat.2017.02.022

588 Baker, D.R., 2008. The fidelity of melt inclusions as records of melt composition. Contrib.
589 Mineral. Petrol. 156, 377–395. https://doi.org/10.1007/s00410-008-0291-3

590 Baker, D.R., Mancini, L., Polacci, M., Higgins, M.D., Gualda, G.A.R., Hill, R.J., Rivers,
591 M.L., 2012. An introduction to the application of X-ray microtomography to the
592 three-dimensional study of igneous rocks. Lithos 148, 262–276.
593 https://doi.org/10.1016/j.lithos.2012.06.008

594 Burkhard, D.J.M., 2005. Nucleation and growth rates of pyroxene, plagioclase, and Fe–Ti
595 oxides in basalt under atmospheric conditions. Eur. J. Mineral. 17, 675–685.
596 https://doi.org/10.1127/0935-1221/2005/0017-0675

597 Cashman, K.V., Mangan, M.T., 2014. A century of studying effusive eruptions in Hawai'i.
598 Characteristics of Hawaiian volcanoes. U.S.G.S. Prof. Paper 1801-9:357–394.
599 http://dx.doi.org/10.3133/pp18019

600 Cashman, K.V., Thornber, C., Kauahikaua, J.P., 1999. Cooling and crystallization of lava in
601 open channels, and the transition of pahoehoe to aa. Bull. Volcanol. 61, 306–323.
602 https://doi.org/10.1007/s004450050299

603 Corrigan, G., 1982. Supercooling and the crystallization of plagioclase, olivine, and
604 clinopyroxene from basaltic magmas. Mineral Mag. 46, 31–42.

605 Corsaro, R.A., Miraglia, L., Pompilio, M., 2007. Petrologic evidence of a complex plumbing
606 system feeding the July–August 2001 eruption of Mt. Etna, Sicily, Italy. Bull.
607 Volcanol. 69, 401–421. https://doi.org/10.1007/s00445-006-0083-4

608 Drakopoulos, M., Connolley, T., Reinhard, C., Atwood, R., Magdysyuk, O., Vo, N., Hart,
609 M., Conner, L., Humphreys, B., Howell, G., Davies, S., Hill, T., Wilkin, G., Pedersen,
610 U., Foster, A., De Maio, N., Basham, M., Yuan, F., Wanelik, K., 2015. J. Synchrotron
611 Rad. 22, 828–838. https://doi.org/10.1107/S1600577515003513

612 Ghiorso, M. S., Sack, R. O., 1995. Chemical mass transfer in magmatic processes IV. A
613 revised and internally consistent thermodynamic model for the interpolation and
614 extrapolation of liquid-solid equilibria in magmatic systems at elevated temperatures
615 and pressures. Contrib. Mineral. Petrol. 119, 197–212.
616 https://doi.org/10.1007/BF00307281

617 Gibb, F.G.F., 1974. Supercooling and the crystallization of plagioclase from a basaltic
618 magma. Min. Mag. 39, 641–653. https://doi.org/10.1180/minmag.1974.039.306.02

619 Giordano, D., Russell, J.K., Dingwell, D.B., 2008. Viscosity of magmatic liquids: a model.
620 Earth Planet Sci. Lett. 271, 123–134. http://dx.doi.org/10.1016/ j.epsl.2008.03.038.

621 Giuliani, L., Iezzi, G., Vetere, F., Behrens, H., Mollo, S., Cauti, F., Ventura, G., Scarlato, P.,
622 2020. Evolution of textures, crystal size distributions and growth rates of plagioclase,
623 clinopyroxene and spinel crystallized at variable cooling rates from a mid-ocean ridge
624 basaltic melt. Earth Sci. Rev. 204:103165.
625 https://doi.org/10.1016/j.earscirev.2020.103165

626 Gürsoy, D., De Carlo, F., Xiao, X., Jacobsen, C., 2014. Tomopy: a framework for the
627 analysis of synchrotron tomographic data. J. Synchrotron Rad. 21, 1188–1193.
628 https://doi.org/10.1107/S1600577514013939

629 Herschel, W.H., Bulkley, R., 1926. Konsistenzmessungen von gummi-benzollösungen.
630 Kolloid-Zeitschrift, 39, 291–300. https://doi.org/10.1007/BF01432034

631 Hon, K.A., Gansecki, C., Kauahikaua, J., 2003. The transition from ʼaʼā to pāhoehoe crust on
632 flows emplaced during the Puʻu ʼŌʼō-Kūpaianaha eruption. USGS Prof. Pap. 1676
633 89–103.

634 Iezzi, G., Mollo, S., Ventura, G., Cavallo, A., Romano, C., 2008. Experimental solidification
635 of anhydrous latitic and trachytic melts at different cooling rates: the role of
636 nucleation kinetics. Chem. Geol. 253, 91–101.

637 Kirkpatrick, R.J., 1975. Crystal growth from the melt: A review. Am. Mineral. 60, 798–814.

638 Kolzenburg, S., Giordano, D., Hess, K.U., Dingwell, D.B., 2018. Shear rate-dependent
639 disequilibrium rheology and dynamics of basalt solidification. Geophys. Res. Lett. 45,
640 6466–6475. https://doi.org/10.1029/2018GL077799

641 Kolzenburg, S., Hess, K.U., Berlo, K., Dingwell, D.B., 2020. Disequilibrium rheology and
642 crystallization kinetics of basalts and implications for the Phlegrean volcanic District.
643 Front. Earth Sci. 8:187. doi: 10.3389/feart.2020.00187

644 La Spina, G., Burton, M. R., de'Michieli Vitturi, M., Arzilli, F., 2016. Role of syn-eruptive
645 plagioclase disequilibrium crystallization in basaltic magma ascent dynamics. Nat.
646 Commun. 7, 13402. https://doi.org/10.1038/ncomms13402

Lanzafame, G., Mollo, S., Iezzi, G., Ferlito, C., Ventura, G., 2013. Unraveling the solidification path of a pahoehoe “cicirara” lava from Mount Etna volcano. Bull. Volcanol. 75, 703. https://doi.org/10.1007/s00445-013-0703-8

Lofgren, G.E., 1983. Effect of heterogeneous nucleation on basaltic textures: a dynamic crystallization study, J. Petrol. 24, 229–255. https://doi.org/10.1093/petrology/24.3.229

Mader, H.M., Llewellin, E.W., Mueller, S.P., 2013. The rheology of two-phase magmas: a review and analysis. J. Volcanol. Geotherm. Res. 257, 135–158. https://doi.org/10.1016/j.jvolgeores.2013.02.014

Mollo, S., Hammer, J.E., 2017. Dynamic crystallization in magmas. EMU Notes Mineral. 16, 373–418. https://doi.org /10.1180/EMU-notes.16.12.

Mollo, S., Giacomoni, P.P., Coltorti, M., Ferlito, C., Iezzi, G., Scarlato, P., 2015. Reconstruction of magmatic variables governing recent Etnean eruptions: constraints from mineral chemistry and P–T–fO_2–H_2O conditions. Lithos 212–215, 311–320.

Mueller, S., Llewellin, E.W., Mader, H.M., 2010. The rheology of suspensions of solid particles. Proceedings of the Royal Society A: Mathematical, Physical and Engineering Sciences, 466(2116), 1201–1228. https://doi.org/10.1098/rspa.2009.0445

Ni, H., Keppler, H., Walte, N., Schiavi, F., Chen, Y., Masotta, M., Li, Z., 2014. In situ observation of crystal growth in a basalt melt and the development of crystal size distribution in igneous rocks. Contrib. Mineral. Petrol. 167, 1–13. https:// doi.org/10.1007/s00410- 014- 1003- 9.

Orlando, A., D’Orazio, M., Armienti, P., Borrini, D., 2008. Experimental determination of plagioclase and clinopyroxene crystal growth rates in an anhydrous trachybasalt from

Mt Etna (Italy). Eur. J. Mineral. 20, 653–664. https://doi.org/ 10.1127/0935-1221/2008/0020- 1841.

Peterson, D.W., Tilling, R.I., 1980. Transition of basaltic lava from pahoehoe to aa, Kilauea Volcano, Hawaii: field observations and key factors. J. Volcanol. Geotherm. Res. 7, 271–293. https://doi.org/10.1016/0377-0273(80)90033-5

Polacci, M., Arzilli, F., La Spina, G., Le Gall, N., Cai, B., Hartley, M.E., Di Genova, D., Vo, N.T., Nonni, S., Atwood, R.C., Llewellin, E.W., Lee, P.D., Burton, M.R., 2018. Crystallisation in basaltic magmas revealed via in situ 4D synchrotron X-ray microtomography. Sci. Rep. 8, 8377–8383. https://doi.org/10.1038/s41598-018-26644-6.

Pontesilli, A., Masotta, M., Nazzari, M., Mollo, S., Armienti, P., Scarlato, P., Brenna, M., 2019. Crystallization kinetics of clinopyroxene and titanomagnetite growing from a trachybasaltic melt: new insights from isothermal time-series experiments. Chem. Geol. 510, 113–129. https://doi.org/10.1016/j.chemgeo.2019.02.015

Rusiecka, M. K., Bilodeau, M., Baker, D. R., 2020. Quantification of nucleation delay in magmatic systems: experimental and theoretical approach. Contribut. Mineral. Petrol. 175:47. https://doi.org/10.1007/s00410-020-01682-4

Schiavi, F., Walte, N., Keppler, H., 2009. First in situ observation of crystallization processes in a basaltic–andesitic melt with the moissanite cell. Geology. 37, 963–966. https://doi.org/10.1130/G30087A.1

Sehlke A., Whittington, A., Robert, B., Harris, A., Gurioli, L., Médard, E., 2014. Pahoehoe to `a`a transition of Hawaiian lavas: an experimental study. Bull. Volcanol. 76, 876. https://doi.org/10.1007/s00445-014-0876-9

693 Soldati, A., Sehlke, A., Chigna, G., Whittington, A., 2016. Field and experimental constraints
694 on the rheology of arc basaltic lavas: the January 2014 Eruption of Pacaya
695 (Guatemala). Bull. Volcanol. 78, 43. https://doi.org/10.1007/s00445-016-1031-6

696 Soldati, A., Beem, J., Gomez, F., Huntley, J.W., Robertson, T., Whittington, A., 2017.
697 Emplacement dynamics and timescale of a Holocene flow from the Cima Volcanic
698 Field (CA): Insights from rheology and morphology. J. Volcanol. Geotherm. Res.
699 347, 91–111. https://doi.org/10.1016/j.jvolgeores.2017.09.005

700 Soule, S.A., Cashman, K.V., Kauahikaua, J.P., 2004. Examining flow emplacement through
701 the surface morphology of three rapidly emplaced, solidified lava flows, Kilauea
702 Volcano, Hawaii. Bull. Volcanol. 66, 1–14.

703 Tamman, G., 1899. Über die abhangigkeidt der zahl der kerne. Z. Phys. Chem. 25, 441–479.

704 Titarenko, V., Titarenko, S., Withers, P.J., De Carlo, F., Xiao, X., 2010. Improved
705 tomographic reconstructions using adaptive time-dependent intensity normalization. J.
706 Synchrotron Radiat. 17, 689–699. https://doi.org/10.1107/S0909049510024908

707 Tripoli, B., Manga, M., Mayeux, J., Barnard, H., 2019. The effects of deformation on the
708 early crystallization kinetics of basaltic magmas. Front. Earth. Sci. 7:250. doi:
709 10.3389/feart.2019.00250

710 Vetere, F., Iezzi, G., Behrens, H., Holtz, F., Ventura, G., Misiti, V., Cavallo, A., Mollo, S.,
711 Dietrich, M., 2015. Glass forming ability and crystallisation behaviour of subalkaline
712 silicate melts. Earth-Sci. Rev. 150, 25–44.
713 https://doi.org/10.1016/j.earscirev.2015.07.001

Vo, N. T., Atwood, R. C., Drakopoulos, M., 2018. Superior techniques for eliminating ring artifacts in X-ray micro-tomography. Opt. Express. 26, 28396–28412. https://doi.org/10.1364/OE.26.028396

Vo, N. T., Drakopoulos, M., Atwood, R. C., Reinhard, C., 2014. Reliable method for calculating the center of rotation in parallel-beam tomography. Opt. Express 22, 19078–19086. https://doi.org/10.1364/OE.22.019078

Vona, A., Romano, C., 2013. The effect of undercooling and deformation on the crystallization kinetics of Stromboli and Etna basalts. Contrib. Mineral. Petrol. 166, 491–509. https://doi.org/10.1007/s00410-013-0887-0

Vona, A., Romano, C., Dingwell, D. B., Giordano, D., 2011. The rheology of crystal-bearing magmas. Geoch. Cosmoch. Acta. 75, 3214–3236. https://doi.org/10.1016/j.gca.2011.03.031

Wentworth, C. K., Macdonald, G. A., 1953. Structures and forms of basaltic rocks in Hawaii. U. S. Geological Survey Bulletin 994, 1–98. https://doi.org/10.3133/b994

Witter, J.B., Harris, A.J.L., 2007. Field measurements of heat loss from skylights and lava tube systems. J. Geophys. Res. 112, B01203. https://doi.org/10.1029/2005JB003800

Figure 1. Sketch of the experimental setup and *in situ* resistance furnace

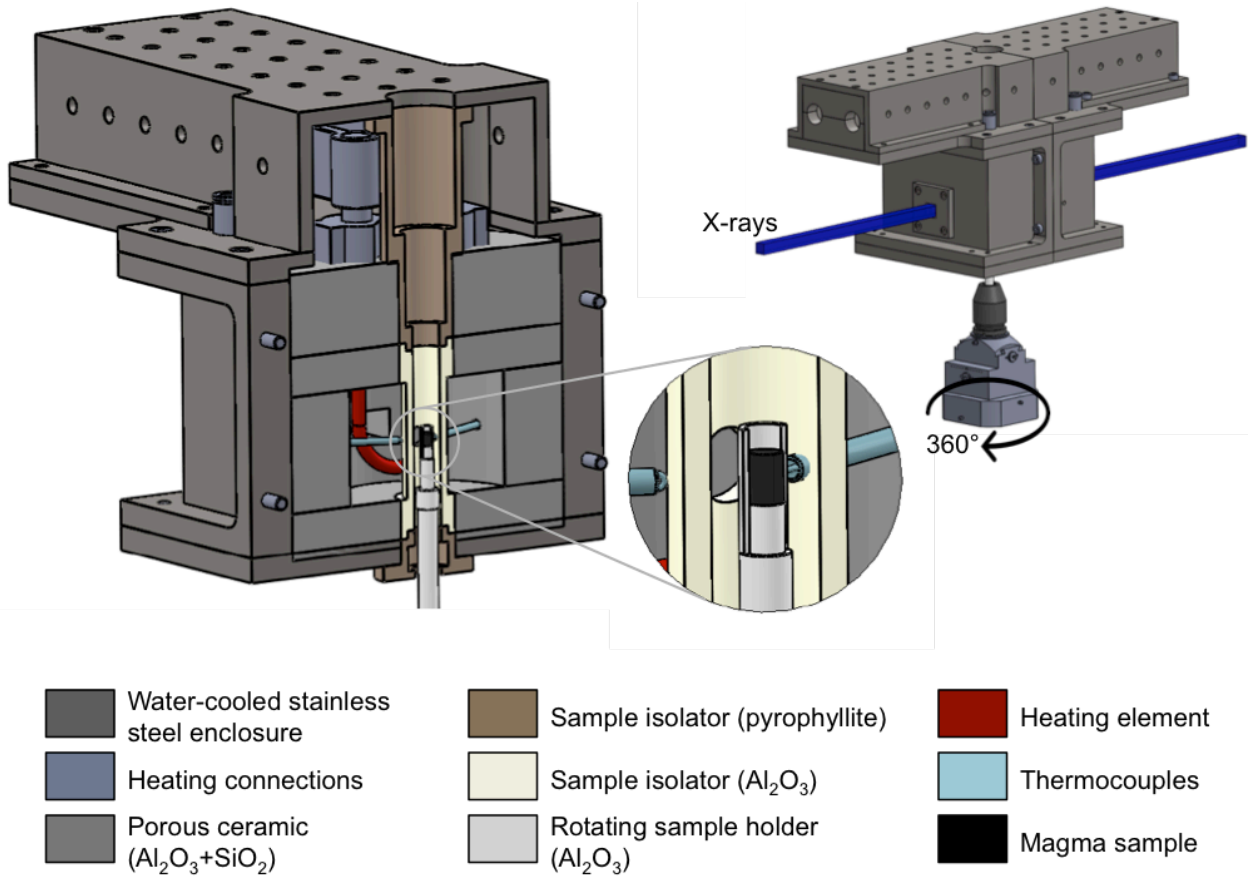

Figure 2. Temperature-time paths followed by the three charges (SSC1170, SSC1150, CC0.5) of this study. t_0: start of the dwell time/cooling, t_1 = 60 min dwell/cooling, t_2 = 160 min dwell/cooling and t_3 = 200 min dwell/cooling. The small (± 5–10 °C) temperature fluctuations are due to sample rotation during image acquisition.

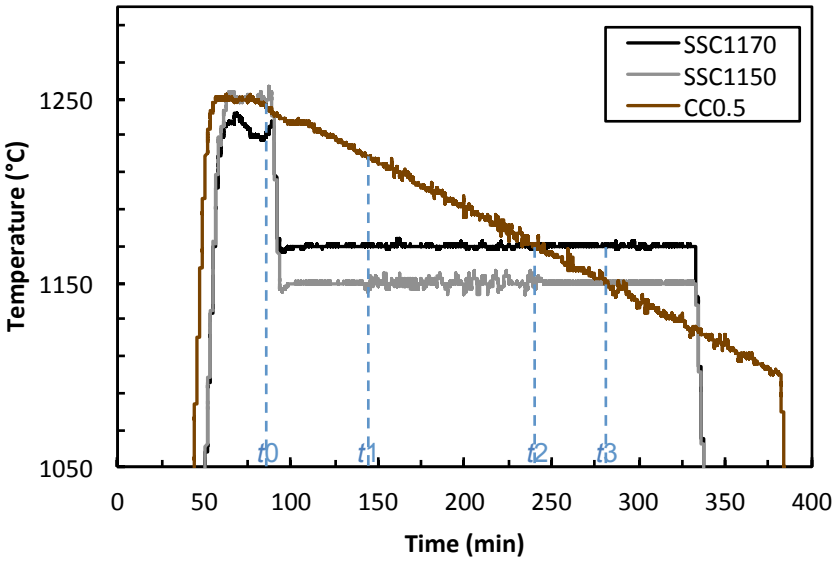

Figure 3. 3D volume renderings of charges SSC1170 (a–c), SSC1150 (d–f) and CC0.5 (g–i) through time, at t_1 = 60 min (a, d, g), t_2 = 160 min (b, e, h) and t_3 = 200 min (c, f, i) after the start of the dwell/cooling time (t_0). In each volume rendering, an orthoslice of the unsegmented dataset is shown in addition to segmented clinopyroxene (Cpx, in light blue) and plagioclase (Plg, in yellow) crystals. The volume fraction of crystals is given in %. Ox: Fe–Ti oxides.

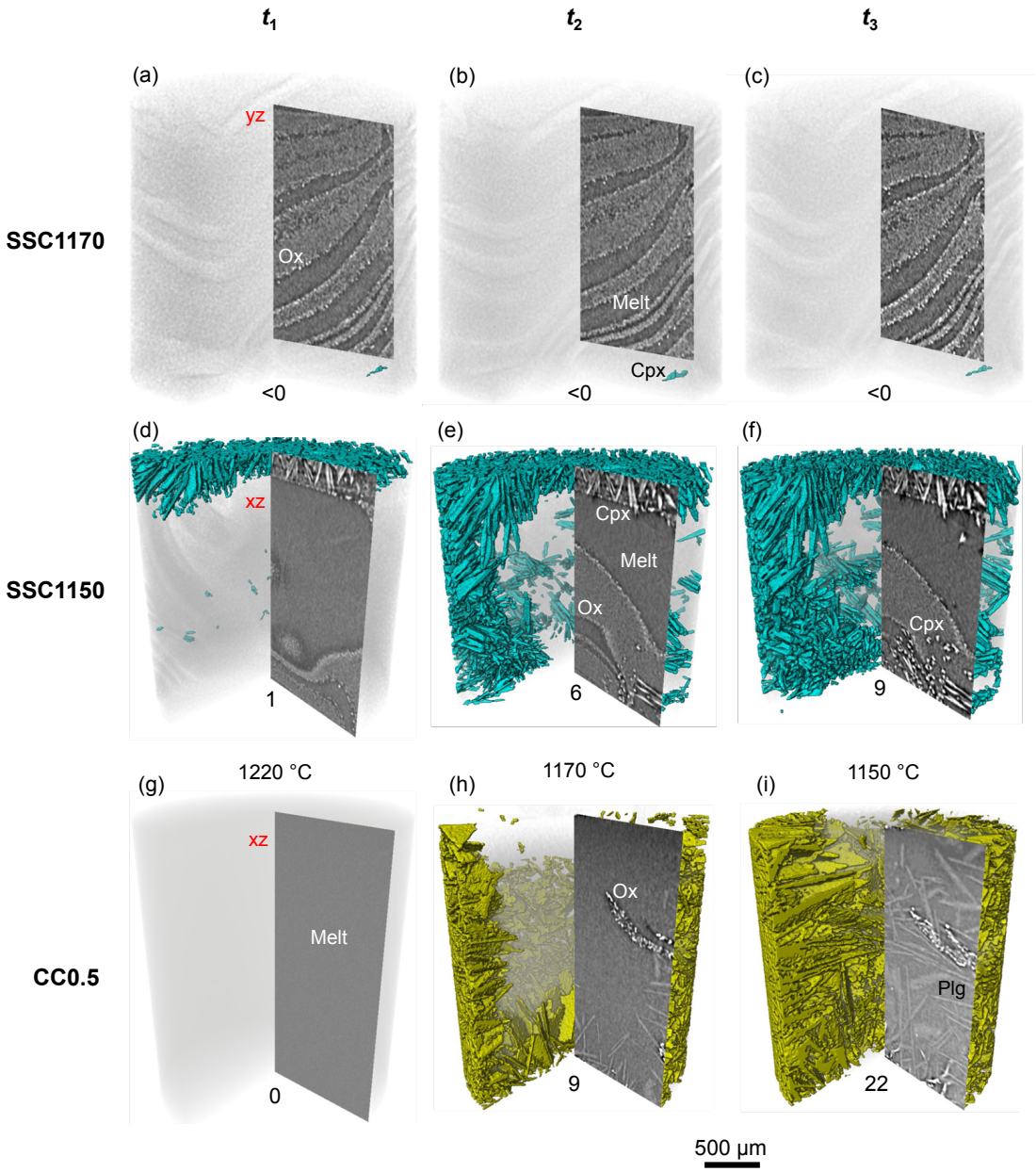

Figure 4. Evolution of (a) clinopyroxene and (b) plagioclase sizes (3D crystal length L_{3D} and volume V) as a function of time and temperature in charges SSC1150 and CC0.5, respectively; t_1, t_2, t_3 = 60, 160, and 200 min dwell/cooling time, respectively. Error bars correspond to the standard deviation of the 3D crystal length/volume of the 10 crystals measured in each sample.

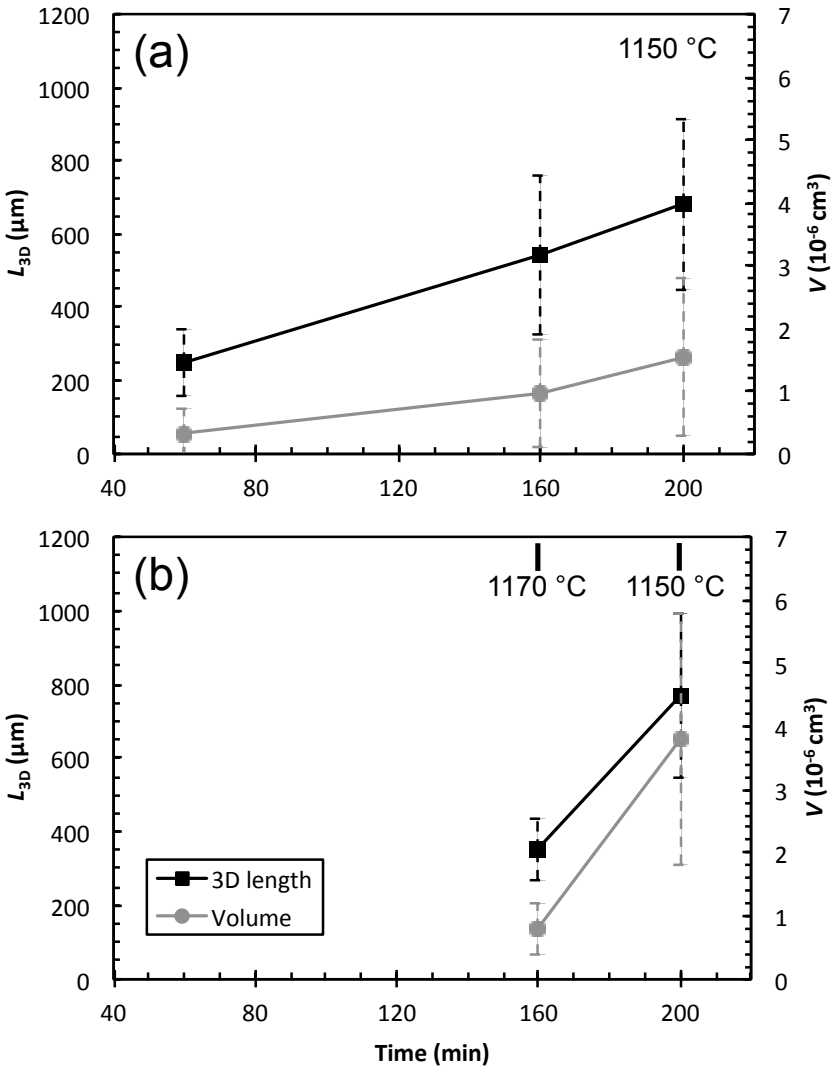

Figure 5. Evolution of crystal growth rates (Y_{L3D} and Y_V) as a function of time and undercooling (ΔT); t_1, t_2, t_3 = 60, 160, and 200 min dwell/cooling time, respectively. Cpx: clinopyroxene crystals in SSC1150; Plg: plagioclase crystals in CC0.5. Error bars represent the standard deviation of the 10 crystals measured in each charge at t_1, t_2 and t_3.

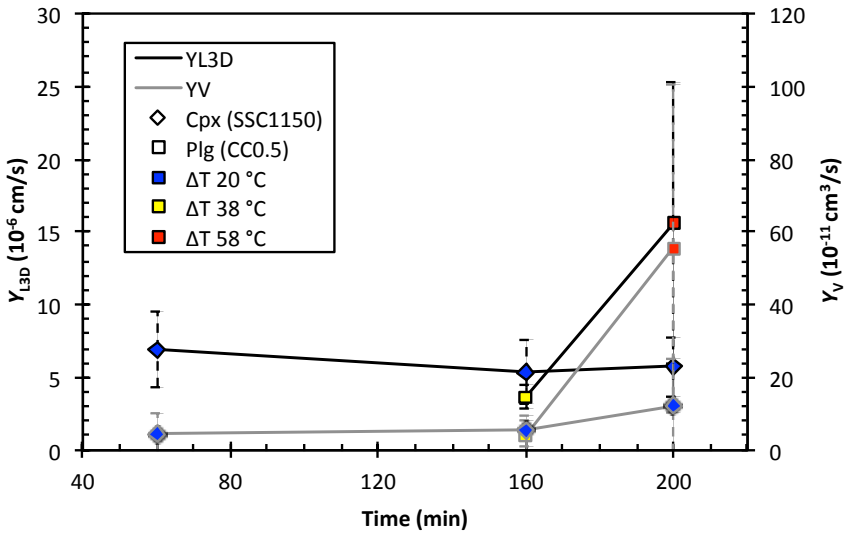

Figure 6. Experimental vs. natural crystal compositons. Data from experiments SSC1170, SSC1150 and CC0.5. Natural data from Corsaro et al. (2007). Mg# (atomic Mg / (Mg + Fe^{2+})) in clinopyroxene crystals; Anorthite content (100 × atomic Ca / (Ca + Na)) in plagioclase crystals.

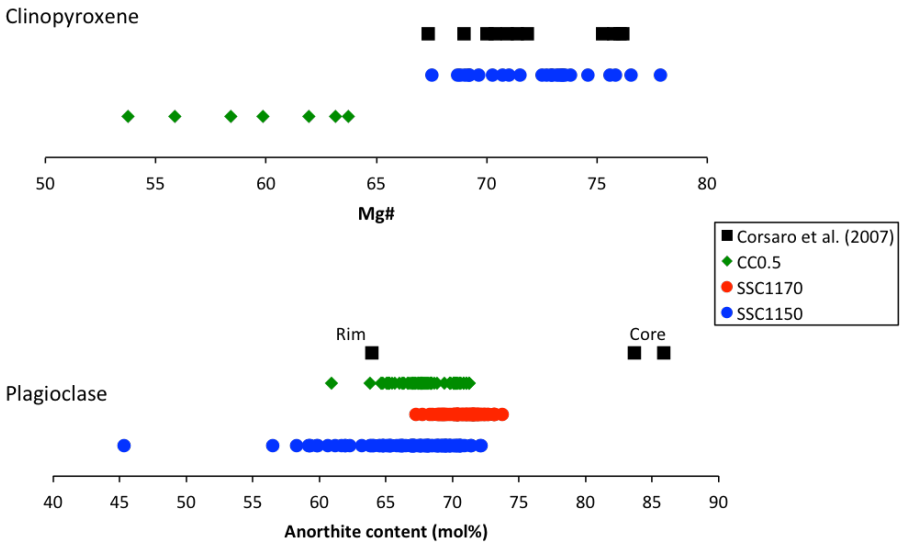

Table 1. Composition of ET01 Lower Vents (LV) volcanics and starting glass, and of phenocrysts

Label	ET01[a] (n = 6)	Glass[b] (n = 23)	Cpx[c] (n = 4)	Plg[c] (n = 3)
SiO_2	47.7 (3)[d]	48.4 (2)	48.7 (17)	48.5 (34)
TiO_2	1.64 (2)	1.79 (7)	1.36 (48)	0.09
Al_2O_3	16.7 (1)	16.2 (5)	4.87 (119)	33.3 (22)
Fe_2O_3	1.77 (2)	nd	nd	nd
FeO	8.84 (11)	10.7 (3)	8.57 (35)	0.62 (15)
MnO	0.17 (0)	0.20 (3)	0.24 (5)	0.02
MgO	6.35 (16)	6.20 (32)	13.2 (11)	0.06 (1)
CaO	11.0 (1)	10.7 (2)	22.0 (7)	15.6 (26)
Na_2O	3.37 (6)	3.41 (20)	0.48 (9)	2.45 (1.30)
K_2O	1.89 (5)	1.90 (7)	nd	0.15 (19)
P_2O_5	0.48 (1)	0.54 (4)	nd	nd
Total	99.2	99.85	99.2	100.8

[a]Whole-rock composition (averaged and normalized to 100% anhydrous) of 2001 Lower Vents (LV) lava flow products, from Corsaro et al. (2007).
[b]Electron microprobe analysis (normalized to 100% anhydrous) of ET01 starting glass, from Arzilli et al. (2019). All Fe reported as FeO.
[c]Electron microprobe analyses of clinopyroxene (Cpx) and plagioclase (Plg) phenocrysts in 2001 LV volcanics, from Corsaro et al. (2007). All Fe reported as FeO.
[d]One standard deviation in terms of last digit unit cited.
n: number of analyses.
nd: not determined.
Oxides are in wt%.

Table 2. Experimental conditions and results

Charge	T_{init} (°C)	T_{exp} (°C)	R (°C/min)	dwell time (min)	ΔT (°C)	Phase assemblage[a]	L_{3D} (cm)	V (cm^3)	Y_{L3D} (cm/s)	Y_V (cm^3/s)
Single-step cooling (SSC)										
SSC1170	1250	1170	24	240	0	gl(92)+ox(8)+cpx(<0.1)	–	–	–	–
SSC1150	1250	1150	24	240	20	gl(83)+ox(8)+cpx(9)	6.8E–02 (2)	1.6E–06 (1)[b]	5.8E–06 (2)	1.2E–10 (1)
Continuous cooling (CC)										
CC0.5	1250	1100	0.5	–	≤108	gl(77)+plg(22)+ox(0.8)	7.7E–02 (2)	3.8E–06 (2)	1.6E–05 (1)	5.5E–10 (5)

Note: T_{init} = initial (or melting) temperature; T_{exp} = experimental (or final) temperature; R = cooling rate; ΔT = undercooling degree, $T_{liquidus} - T_{experimental}$ with $T_{liquidus}$ = 1208 °C for plagioclase and $T_{liquidus}$ = 1170 °C for clinopyroxene; L_{3D} = crystal length; V = crystal volume; Y_{L3D} = crystal growth rate = L_{3D}/t_{exp} with t_{exp} the experimental duration (in s, Arzilli et al., 2015); Y_V = volumetric growth rate = $(V\times0.5)/t_{exp}$ (Arzilli et al., 2015); r_p = crystal length/width aspect ratio; ϕ_m = maximum crystal packing fraction; ϕ/ϕ_m = ratio of the crystal volume fraction to the maximum crystal packing fraction, κ = consistency; n = flow index. All textural parameters are averaged over 10 selected crystals at t_3 (after 200 min of dwell/cooling).

[a]Phase proportions calculated by 3D image analysis at t_3; gl, glass; cpx, clinopyroxene; plg, plagioclase; ox, Fe–Ti oxide. In SSC1150, the oxide contents were calculated to be 4 vol% and 8 vol% at t_1 and t_2, respectively.

[b]Standard deviation of the mean value.

Charge	r_p	ϕ_m	ϕ/ϕ_m	κ	n
Single-step cooling (SSC)					
SSC1170	–	–	–	–	–
SSC1150	7.35 (3)	0.38	0.24	1.72	1
Continuous cooling (CC)					
CC0.5	5.76 (2)	0.41	0.53	4.60	0.91

Fig. A.1. Longitudinal (XZ) slices through the 3D volume renderings of charges (a) CC0.5, (b) SSC1150 and (c) SSC1170 showing the heterogeneous nucleation of crystals (Plg: plagioclase, Cpx: clinopyroxene) after 60 min of cooling/dwell (t_1). Ox: oxide. The volume of interest (VoI, red inset) selected for quantitative image analysis is depicted in (a). In (c) a transverse (XY) slice of the SSC1170 charge is also depicted.

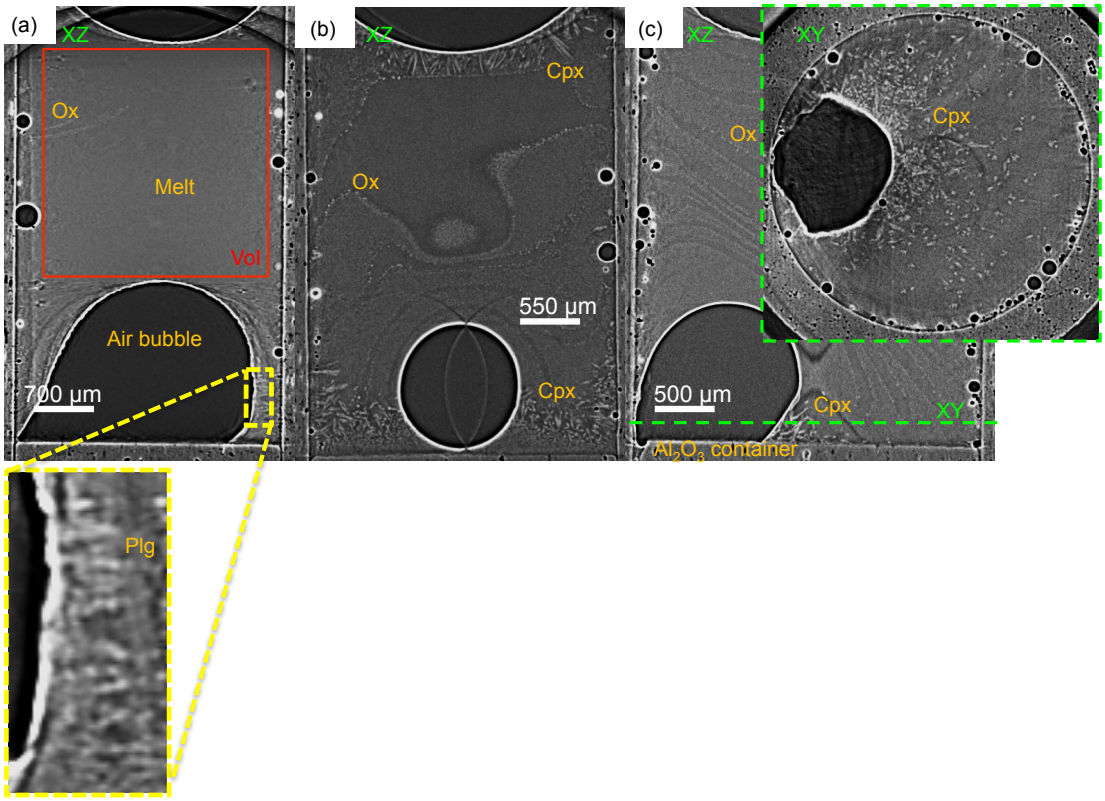

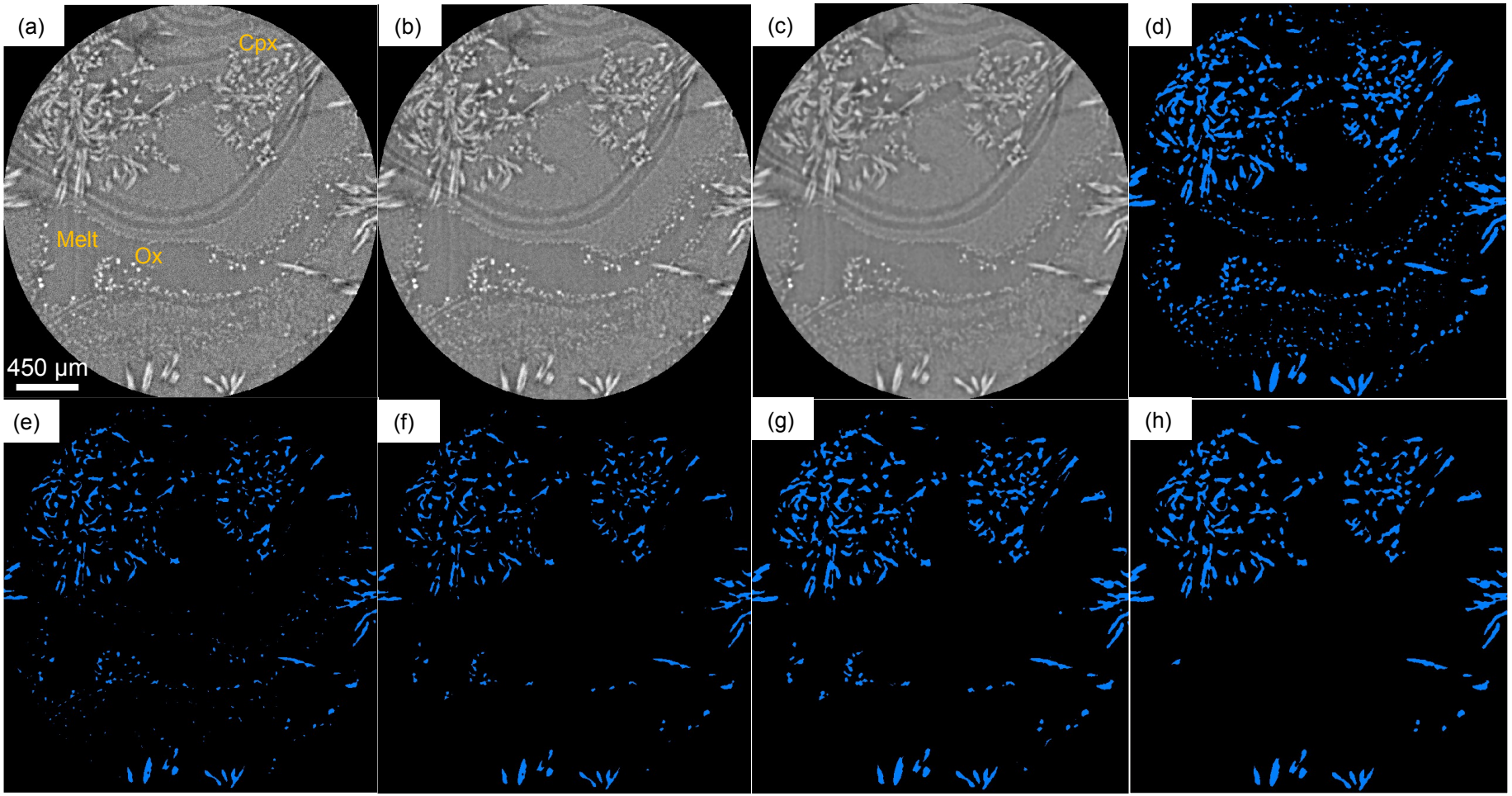

Fig. A.2. Overview of the image analysis procedure using Avizo. A transverse (XY) slice through the 3D volume rendering of the SSC1150 charge after 160 min of dwell (t_2) is shown for illustration. (a) Initial stage, after pre-processing with ImageJ; (b) After bilateral filtering; (c) After median filtering; (d) After interactive thresholding; (e) After erosion; (f) After removing small spots; (g) After dilation; (h) Final stage, after manual correction. Cpx: clinopyroxene; Ox: oxide.

Fig. A.3. Selected clinopyroxene (a) and plagioclase (b) crystals in samples SC1150 and CC0.5, respectively. Scale bars: 200 μm.

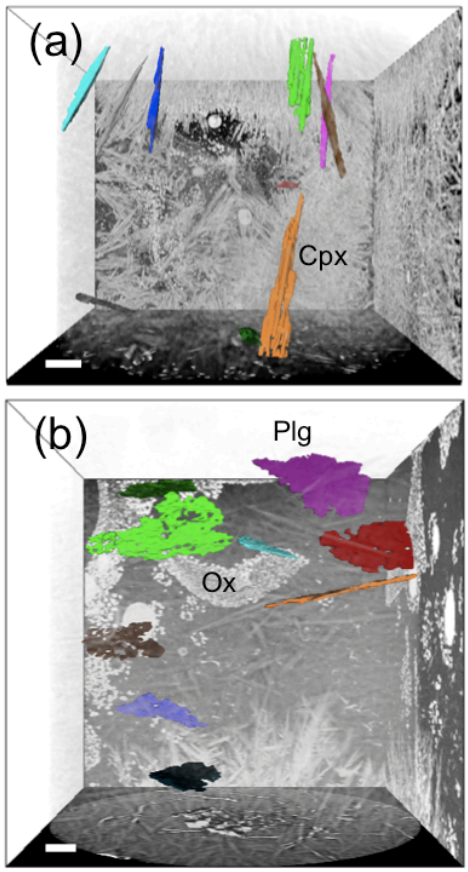

Fig. A.4. (a) SEM image of a test sample showing the formation of an oxide layer on the edge of an alumina container. The sample is a basalt from the Mt. Etna eruption of 2001 that has been left 5 hours in air, at 1 atm and 1190 °C before being air-quenched. (b) ESD analyses demonstrating that the oxides are made of Al and Mg. Ox: oxide; plg: plagioclase; cpx: clinopyroxene.

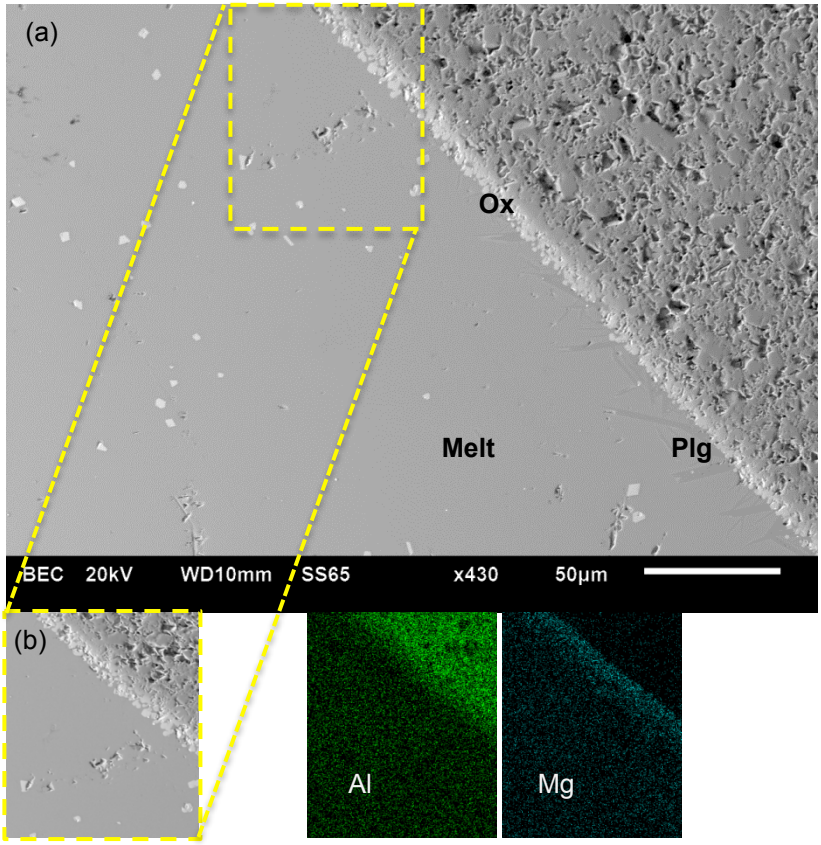

Table A.1. Experimental compositions

Charge	Phase	SiO_2	TiO_2	Al_2O_3	FeO	MnO	MgO	CaO	Na_2O	K_2O	P_2O_5	Cr_2O_3	NiO	Total	Mol%
SSC1170	gl[a](3)[b]	50.6(4) [c]	1.85(6)	15.8(1)	8.52(11)	0.22(4)	6.25(1)	11.3(2)	3.41(9)	1.50(16)	0.52(7)	0.03(1)	0.03(1)	98.0	
SSC1150	gl(10)	53.4(4)	1.73(3)	18.1(2)	5.90(16)	0.18(1)	4.77(16)	7.97(24)	4.91(7)	2.84(10)	nd	0.01(0)	0.01(0)	96.2	
	cpx(26)	42.7(12)	1.88(29)	7.97(86)	9.21(69)	0.17(2)	13.3(8)	21.0(3)	0.47(3)	0.01(1)	nd	0.01(1)	0.01(1)	96.8	$En_{45}Wo_{40}$
CC0.5	gl(8)	53.8(12)	2.11(20)	14.9(7)	7.13(88)	0.24(8)	5.37(56)	7.57(67)	4.49(58)	3.53(40)	0.85(17)	0.02(1)	0.02(0)	98.2	
	plg(69)	51.1(8)	0.14(4)	27.6(6)	2.99(28)	0.03(2)	0.22(10)	13.4(4)	3.49(24)	0.41(7)	0.05(5)	0.02(1)	0.02(1)	99.3	$An_{68}Or_7$

[a]Glass analyses normalized to 100% anhydrous, with all Fe as FeO.
[b]Number of microprobe analyses.
[c]One standard deviation in terms of last digit unit cited.
n: number of analyses.
nd: not determined.
gl, glass; cpx, clinopyroxene; plg, plagioclase. Enstatite En = 100 × at. Mg / (Mg + Fe + Ca); Wollastonite Wo = 100 × at. Ca / (Mg + Fe + Ca) in pyroxene, calculated with Fe = FeO; Anorthite An = 100 × at. Ca / (Ca + Na); Orthoclase Or = 100 × at. K / (K + Na) in plagioclase.

Table A.2. 3D clinopyroxene crystal measurements

Crystal	Time	L_{3D} (cm)	Y_{L3D} (cm/s)	V (cm^3)	Y_V (cm^3/s)	r_p
cpx-01	t_1	0.032	9.0E-06	1.0E-06	1.4E-10	2.22
	t_2	0.063	5.1E-06	2.7E-06	1.4E-10	3.58
	t_3	0.069	2.4E-06	2.9E-06	3.0E-11	3.61
cpx-02	t_1	0.032	8.8E-06	2.4E-07	3.4E-11	5.31
	t_2	0.074	7.0E-06	9.5E-07	5.9E-11	12.6
	t_3	0.087	5.4E-06	1.5E-06	1.1E-10	11.1
cpx-03	t_1	0.026	7.2E-06	2.5E-07	3.5E-11	5.69
	t_2	0.049	3.8E-06	6.3E-07	3.1E-11	7.08
	t_3	0.071	9.2E-06	9.7E-07	7.2E-11	7.89
cpx-04	t_1	0.026	7.1E-06	1.2E-07	1.6E-11	–
	t_2	0.068	7.1E-06	6.4E-07	4.4E-11	14
	t_3	0.079	4.4E-06	9.7E-07	6.9E-11	12.4
cpx-05	t_1	0.009	2.5E-06	4.1E-08	5.8E-12	3.05
	t_2	0.036	4.4E-06	5.2E-07	4.0E-11	4.26
	t_3	0.05	6.1E-06	1.0E-06	1.1E-10	4.99
cpx-06	t_1	–	–	–	–	–
	t_2	0.089	9.2E-06	2.3E-06	1.2E-10	5.54
	t_3	0.109	8.4E-06	4.6E-06	4.9E-10	6.03
cpx-07	t_1	–	–	–	–	–
	t_2	0.062	6.5E-06	6.4E-07	3.3E-11	10.1
	t_3	0.079	6.9E-06	1.1E-06	1.1E-10	11
cpx-08	t_1	–	–	–	–	–
	t_2	0.055	5.7E-06	8.9E-07	4.7E-11	7.19
	t_3	0.064	4.0E-06	1.2E-06	7.3E-11	7.36
cpx-09	t_1	–	–	–	–	–
	t_2	0.032	3.3E-06	2.7E-07	1.4E-11	5.75
	t_3	0.047	6.3E-06	7.7E-07	1.0E-10	5.88
cpx-10	t_1	–	–	–	–	–
	t_2	0.015	1.5E-06	9.5E-08	5.0E-12	3.97
	t_3	0.025	4.4E-06	4.3E-07	7.0E-11	3.24

cpx, clinopyroxene; L_{3D} = 3D crystal length; Y_{L3D} = crystal growth rate; V = crystal volume; Y_V = volumetric crystal growth rate; r_p = crystal aspect ratio (= length/width ratio). t_1, t_2, t_3 = 60, 160, and 200 min dwell, respectively.

Note that at t_2 growth rates are calculated for the time interval between t_1 and t_2 and at t_3 the rates are calculated for the t_2–t_3 time interval.

These single measurements are assumed to contain an error of 10% because of variation in the segmentation threshold.

Table A.3. 3D plagioclase crystal measurements

Crystal	Time	L_{3D} (cm)	Y_{L3D} (cm/s)	V (cm^3)	Y_V (cm^3/s)	r_p
plg-01	t_2	0.052	5.4E-06	1.3E-06	6.7E-11	4.40
	t_3	0.101	2.0E-05	6.2E-06	1.0E-09	4.36
plg-02	t_2	0.045	4.7E-06	1.6E-06	8.2E-11	4.90
	t_3	0.058	5.5E-06	2.8E-06	2.6E-10	6.21
plg-03	t_2	0.038	4.0E-06	1.0E-06	5.2E-11	3.71
	t_3	0.070	1.3E-05	2.9E-06	4.0E-10	4.20
plg-04	t_2	0.035	3.7E-06	6.0E-07	3.1E-11	3.98
	t_3	0.065	1.2E-05	2.5E-06	3.9E-10	4.64
plg-05	t_2	0.034	3.6E-06	9.6E-07	5.0E-11	4.17
	t_3	0.059	1.0E-05	2.3E-06	2.8E-10	5.10
plg-06	t_2	0.031	3.2E-06	3.4E-07	1.8E-11	6.08
	t_3	0.090	2.5E-05	3.9E-06	7.5E-10	9.63
plg-07	t_2	0.028	2.9E-06	5.8E-07	3.0E-11	3.90
	t_3	0.045	6.9E-06	1.5E-06	1.9E-10	3.87
plg-08	t_2	0.028	2.9E-06	4.1E-07	2.1E-11	3.49
	t_3	0.116	3.7E-05	8.1E-06	1.6E-09	6.45
plg-09	t_2	0.027	2.8E-06	4.0E-07	2.1E-11	3.49
	t_3	0.072	1.9E-05	2.6E-06	4.5E-10	9.11
plg-10	t_2	–	–	–	–	–
	t_3	0.095	8.0E-06	4.9E-06	2.0E-10	3.98

plg, plagioclase; L_{3D} = 3D crystal length; Y_{L3D} = crystal growth rate; V = crystal volume; Y_V = volumetric crystal growth rate; r_p = crystal aspect ratio (= length/width ratio). t_1, t_2, t_3 = 60, 160, and 200 min cooling time, respectively.

Note that at t_2 growth rates are calculated for the time interval between t_1 and t_2 and at t_3 the rates are calculated for the t_2–t_3 time interval.

These single measurements are assumed to contain an error of 10% because of variation in the segmentation threshold.

Credit Author Statement

M.P., M.R.B., F.A. and P.D.L. conceived the research project. All authors, N.L.G., F.A., G.L.S., M.P., B.C., M.E.H., N.T.V., R.C.A., D.D.G., S.N., E.W.L., M.R.B. and P.D.L. contributed to the beamline experiments. F.A. collected the volcanic rocks for the starting material. D.D.G. prepared the starting material. F.A., M.P., G.L.S. and N.T.V. performed image reconstruction. N.L.G. performed image processing with help from F.A. and M.P. N.LG. performed the image segmentation and analysis. F.A. and M.E.H. performed chemical analysis. N.L.G. wrote the manuscript, with contributions from all other authors.